ELSEVIER

Tectonophysics 304 (1999) 201–218

TECTONOPHYSICS

3D crustal structure from local earthquake tomography around the Gulf of Arta (Ionian region, NW Greece)

F. Haslinger [a,*], E. Kissling [a], J. Ansorge [a], D. Hatzfeld [b], E. Papadimitriou [c], V. Karakostas [c], K. Makropoulos [d], H.-G. Kahle [e], Y. Peter [e]

[a] *Institute of Geophysics, ETH Zürich, Switzerland*
[b] *LGIT, Université Joseph Fourier, Grenoble, France*
[c] *Geophysical Laboratory, University of Thessaloniki, Thessaloniki, Greece*
[d] *Department of Geophysics, University of Athens, Athens, Greece*
[e] *Institute of Geodesy and Photogrammetry, ETH Zürich, Switzerland*

Received 27 May 1998; revised version received 9 December 1998; accepted 9 December 1998

Abstract

During summer of 1995 local seismicity was recorded in the area around the Gulf of Arta in northwestern Greece by a dense temporary seismic network. Of the 441 local events observed at 37 stations, 232 well locatable events with a total of 2776 P-phase readings were selected applying the criteria of a minimum of 6 P-observations and an azimuthal gap less than 180°. This data set is used to compute a minimum 1D velocity model for the region. Several tests are conducted to estimate model stability and hypocenter uncertainties, leading to the conclusion that relative hypocenter location accuracy is about 500 m in latitude and longitude and 1 km in depth. The minimum 1D velocity model serves as initial model in the non-linear inversion for three-dimensional P-velocity crustal structure by iteratively solving the coupled hypocenter–velocity problem in a least-squares sense. Careful analysis of the resolution capability of our data set outlines the well resolved features for interpretation. The resulting 3D velocity model shows generally higher average crustal velocities in the east, and the well resolved area of the eastern Gulf of Arta exhibits a homogeneous velocity around 6 km/s for the whole upper crust. A pronounced north–south trending zone of low velocities in the upper 5–10 km is observed in the area of the Katouna fault zone (KFZ). At greater depths (below 10 km) the KFZ is underlain by high-velocity material. E–W profiles suggest a horst–graben structure associated with the KFZ.

Keywords: NW Greece; seismicity; crustal structure; seismic tomography

1. Introduction

The neotectonic regime of the Ionian region of Greece is governed by relative motions between the Eurasian and African plates and the Aegean and Adriatic microplates (Fig. 1). Africa, the Adriatic and the Aegean form a triple junction in the Ionian Sea, where the dextral strike-slip Cefalonia fault (CF) hits the front of the Hellenic subduction zone (Sachpazi et al., 1999). On the Greek mainland the boundary between Eurasia and the Aegean is not well defined. The Ionian region exhibits some of the largest observed rates of continental crustal defor-

* Corresponding author. Tel.: +41-1-633-6773; Fax: +41-1-633-1065; E-mail: haslinger@tomo.ig.ethw.ethz.ch

0040-1951/99/$ – see front matter
PII: S0040-1951(98)00298-4

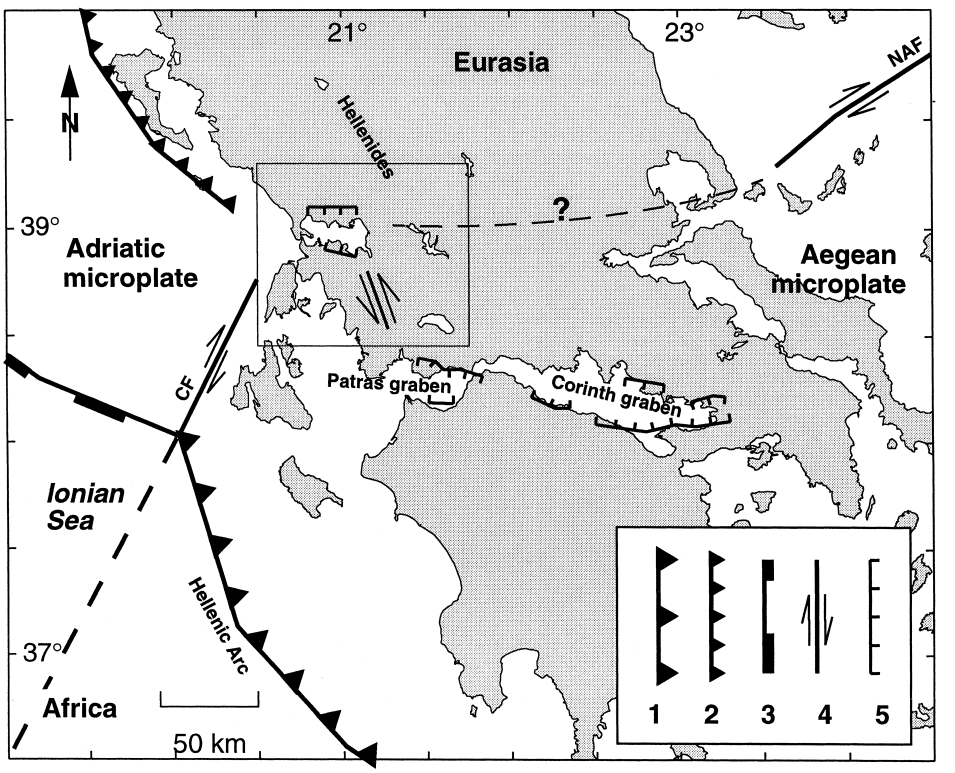

Fig. 1. Simplified tectonic structure of the east-central Mediterranean region (modified from Reuther et al., 1993; Hatzfeld et al., 1995; Mantovani et al., 1997; Armijo et al., 1996). *1* = subduction; *2* = continental collision; *3* = Mesozoic passive margin; *4* = strike-slip fault; *5* = normal fault. *NAF* = North Anatolian fault (western continuation); *CF* = Cefalonia fault. The more detailed tectonics of the study area are shown in Fig. 2 (area of Fig. 2 marked by box).

mation accompanied by very high seismic activity. Numerous regional studies have been carried out to assess the geodynamics of this area from seismological, geodetic and neotectonic points of view (e.g. Brooks et al., 1988; King et al., 1993; Melis et al., 1995; Kahle et al., 1993, 1995; Le Pichon et al., 1995; Hatzfeld et al., 1995).

Active tectonics in the study area (Fig. 2) are mostly extensional, due to the relative motion between the Eurasian–Adriatic plates to the north and the fast southwestward moving Aegean microplate. The Gulf of Arta region is interpreted as a north–south pull-apart basin (e.g. King et al., 1993; Le Pichon et al., 1995). The Katouna fault zone (KFZ, Fig. 2) connects the well documented active extensional graben systems of the Gulf of Corinth–Gulf of Patras with the Arta basin, requiring sinistral strike-slip motion along the KFZ. Hatzfeld et al. (1995), however, did not find conclusive seismological evidence in their earthquake mechanisms for the spreading around the Gulf of Arta nor for a sinistral motion on the KFZ.

Our field experiment was aimed to collect a high-quality local earthquake data set that would allow the derivation of models of the three-dimensional (3D) crustal structure and the seismotectonic regime, thereby adding more constraints to define and consistently interpret the extent and motion of the crustal blocks in this region. Here we report on first results obtained by high-resolution seismic tomography using local earthquake data.

2. Method

In a first step a minimum 1D velocity model (Kissling, 1988) was computed. A minimum 1D velocity model with corresponding station correc-

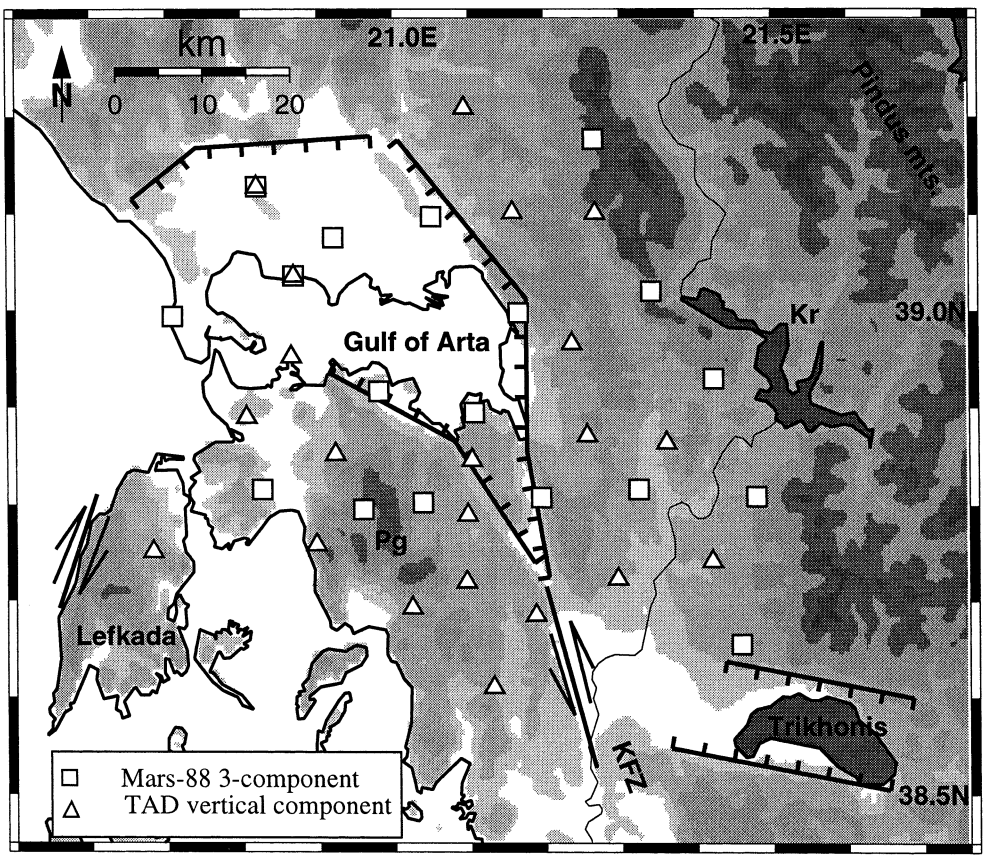

Fig. 2. Map of the study area with topography in grey shading (bathymetry always above 200 m) and simplified main tectonic elements. The temporary seismic network is represented by white symbols. *KFZ* = Katouna fault zone; *Pg* = Pergandi Mountains; *Kr* = Kremaston reservoir. Tectonic elements compiled from, King et al. (1993), Melis et al. (1995) and Hatzfeld et al. (1995). See Fig. 1 for fault signature.

tions results from simultaneous inversions of a large number of travel times from selected high-quality events for both model and hypocenter parameters. It is designed to locate these events with the smallest possible uniform location error. The calculation of a minimum 1D model, following the routine procedure as defined in the Velest Users Guide (Kissling, 1995) and by Kissling et al. (1994), is a trial and error procedure for different initial velocity models, initial hypocenter locations, and damping and control parameters for the coupled inverse problem. The term 'uniform location error' denotes that the sum of residuals for all events is minimized in the joint inversion. In a sense, the location accuracy is then relative to the full data set (Kissling et al., 1995). Without additional information, like quarry blasts, the absolute location accuracy can normally not be assessed. For a set of well-locatable events with an azimuthal gap (the largest angular distance between two neighboring stations as seen from the epicenter) $\leq 180^{o}$, and at least six P-observations, which are evenly distributed within a network, the absolute location uncertainty can be approximately estimated by using randomly and systematically shifted hypocenters as initial locations and by analyzing the differences in final locations. In addition to these tests of hypocenter location accuracy, several tests have been conducted to assess the quality of the 1D velocity model.

In a second step the same data set is inverted for the 3D crustal P-velocity structure by local earthquake tomography (LET). LET denotes the process

of iterative simultaneous inversion for 3D velocity structure and hypocenter parameters using travel-time residuals from local earthquakes. In this work we use a version of the SIMULPS code originally written by Thurber (1983), which performs the inversion by a damped least-squares approach and implements a grid-parameterization of the velocity model, where velocity values are defined at grid-nodes and are linearly interpolated between nodes. To solve the forward problem, approximate 3D ray-tracing (Thurber, 1983) and pseudo-bending (Um and Thurber, 1987) is applied. Hypocenter locations are updated within the new velocity model at each iteration step.

The minimum 1D model is used to derive the initial 1D reference velocity model for LET, since this meets the statistical requirements imposed by the implicit linearization in the inversion scheme (Kissling et al., 1994). Although the minimum 1D model is a layered model with constant layer velocities and the initial 1D model for the LET is a gradient model, Kissling et al. (1994) showed the equivalence of these models when they are adequately parameterized. To derive the initial reference model from a minimum 1D model yields the most appropriate initial model for LET (e.g. Evans et al., 1994). For a detailed description of LET methodology the reader is referred to Eberhart-Phillips (1986, 1993), Kissling (1988) and Thurber (1993).

3. Local earthquake data

18 three-component (ETH Zurich Lennartz Mars88 equipped with Le3D 1 Hz sensors) and 21 vertical-component stations (LGIT-Grenoble TAD equipped with L-22D 2 Hz sensors) were installed at the beginning of July 1995 around the Gulf of Arta in an area of about 100 × 80 km (Fig. 2). The network was operated until the end of September 1995, recording 441 locatable local (within ∼50 km around the network) events (Fig. 3) encompassing a data set of 5145 P- and 1909 S-phases. S-phases were almost exclusively picked on three-component stations, which explains the smaller number of S-picks. Data were recorded with a sampling rate of 100 Hz for the TAD and 250 Hz for the Mars88 stations. The average time uncertainty for P-phase-picks for this data set is less than 0.05 s. Station coordinates were obtained by GPS measurements and from maps with a horizontal accuracy of ±100 m and a vertical accuracy of ±50 m.

4. Minimum 1D model and station delays

At first only P-phases were used for the computation of a minimum 1D model as they provide better spatial sampling of the subsurface and have smaller picking errors and thus will lead to a more stable solution. With the criteria of at least 6 P-observations and a gap $\leq 180^{o}$, a data set of 232 well-locatable events with a total of 2928 P-observations was selected (Fig. 3). Due to the dimensions of the recording array (approx. 80 km by 100 km) and the depth distribution of the earthquakes with almost no seismic activity below 25 km, the Moho is only poorly resolved by our data. Therefore, a Moho depth of about 40 km (Hatzfeld et al., 1995; Papazachos et al., 1995) and a P_n-velocity of 8.0–8.2 km/s, as inferred from a travel-time plot for an event of the Hatzfeld '95 data set (Hatzfeld et al., 1995), was used as a priori information. Initial average crustal velocity was taken from the model obtained by Hatzfeld et al. (1995) for a larger region encompassing our study area. We started the 1D inversion with a large number of thin layers (∼2 km thick), and during the inversion process combined those layers for which velocities converged to similar values. The final layering of the minimum 1D model emerged from this process.

The final minimum 1D P-velocity model (Fig. 3; Table 1) and station delays reduced the data RMS residual by 60% from 0.2 s to 0.08 s. A series of tests to assess the quality of this 1D P-velocity model was then carried out. The inversion was started using initial models with average velocities significantly higher or lower than the minimum 1D P-model and with event locations which were perturbed randomly in their three spatial coordinates. To create this randomized input data, every hypocenter is shifted ±6 to 8 km in each direction (x, y, z), with the actual shift-value drawn from a random distribution. Shallow events, which would thereby be moved above the surface, are shifted downwards. Thus the randomized input data are biased for events in the upper 8 km

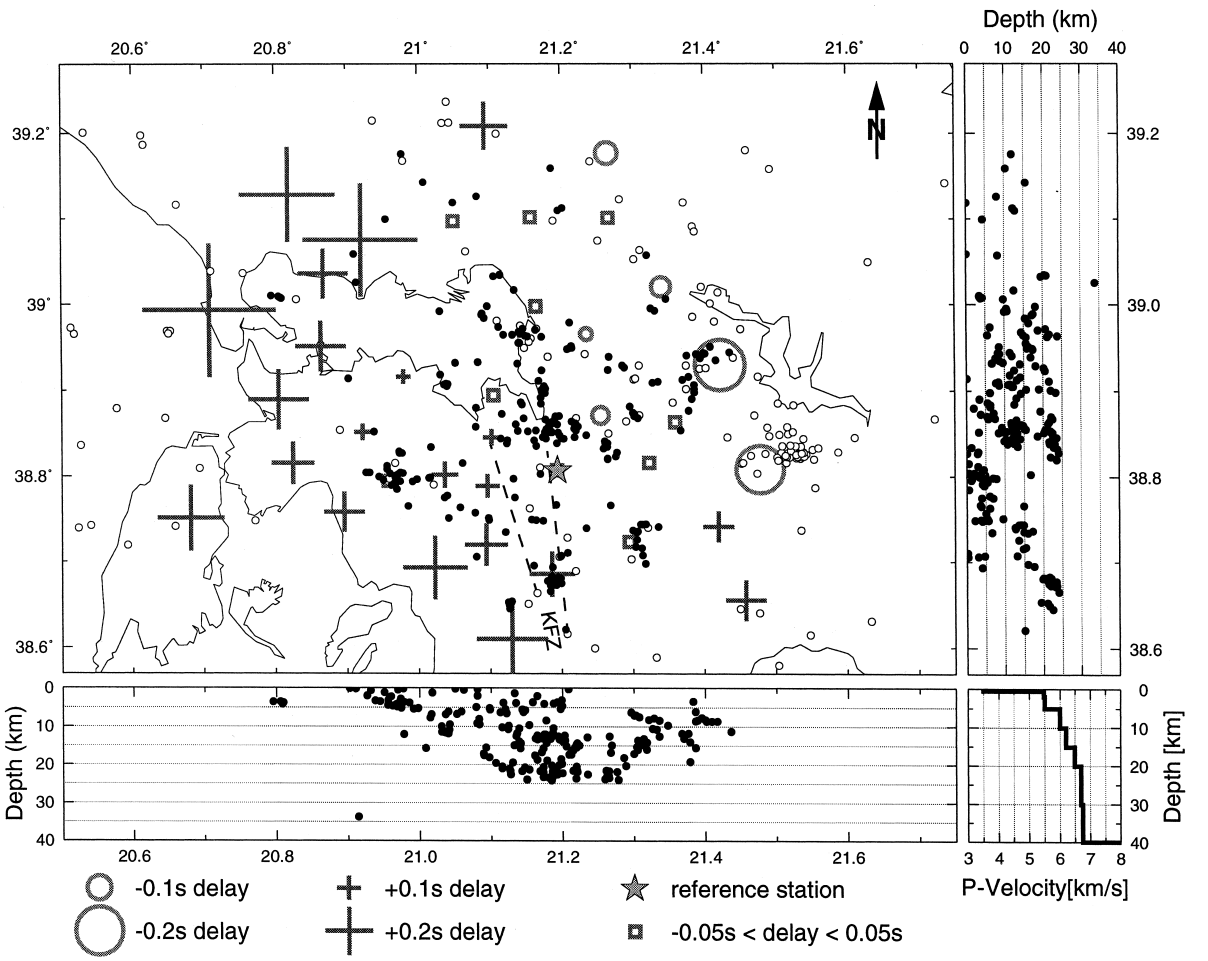

Fig. 3. Distribution of seismicity and the minimum 1D P-velocity model with corresponding station delays. Small full circles on map and depth-sections are well locatable events (gap <180°, P-observations ≥6) which have been used to invert for a minimum 1D model. Open circles are the remaining local events recorded during the experiment. The final minimum 1D P-velocity model is shown in the lower right corner. Dark grey crosses and light grey open circles on the map show the station delays relative to the reference station obtained with the minimum 1D model. Negative delays correspond to true velocities faster than the model, positive delays to true velocities slower than the model. Delays with absolute values less than 0.05 s are shown as open squares. E–W and N–S depth cross-sections show all well locatable events projected on them (vertical exaggeration approx. ×2).

towards deeper events compared to the initial data. This bias is retained in the relatively large average depth difference for the output of these tests (+964 m for the P-data and +928 m for the P- + S-data). A part of this systematic depth difference is compensated by increasing the velocity in the 2–5 km layer (Fig. 4) and systematically enlarging the station delays, +0.05 s on the average. In general, though, the hypocenter locations are well recovered (Table 2; Fig. 6). With regard to the velocity model, these tests show (Fig. 4) that — as expected — the top layer (surface to 0.5 km depth) is not constrained by the data since the effect of locally varying velocities may be compensated by station delays, and systematic shifts in station delays as well as event depths can account for different layer velocities. From the second layer down to 20 km velocities are well constrained, as documented by the results for different input models that converge to within 0.2–0.3 km/s of the minimum 1D P-model. Between 20 and 30 km depth the velocity uncertainty increases and below 30 km the model is again poorly constrained due to

Table 1
Tabulated values for the minimum 1D velocity model for the Gulf of Arta region, NW Greece, for P- and S-wave velocities with error estimates

Depth (km)	V_p (km/s)	V_s (km/s)
<0.5 [a]	3.5	1.9
0.5–2.0	5.47 ± 0.1	2.7 ± 0.1
2.0–5.0	5.50 ± 0.1	2.86 ± 0.1
5.0–10.0	6.0 ± 0.2	3.23 ± 0.2
10.0–15.0	6.2 ± 0.2	3.24 ± 0.2
15.0–20.0	6.48 ± 0.25	3.40 ± 0.2
20.0–30.0	6.70 ± 0.4	3.80 ± 0.25
30.0–40.0 [b]	6.75	3.81
>40.0 [c]	8.0	–

[a] No error estimate for top layer, velocities unconstrained due to strong coupling with station delays.
[b] Velocities below 30 km are poorly constrained due to the sparse sampling.
[c] P_n velocity and Moho depth based on a priori information.

Table 2
Standard errors (upper value) and average difference (lower value) for hypocentral locations comparing the randomized event output for P only, the minimum 1D P + S output to the minimum 1D P output, the randomized event output for P + S to the minimum 1D P + S output, and the 3D P-velocity tomography output to the minimum 1D P output

	σ (m)		
	Average difference (m)		
	longitude	latitude	depth
Randomized events output P only– minimum 1D P output	446 1231	535 −261	1210 964
Minimum 1D P + S output– minimum 1D P output	441 −229	351 67	992 80
Randomized events output P + S– minimum 1D P + S output	362 227	459 −232	904 928
3D P tomography output– minimum 1D P output	363 190	351 124	852 −293

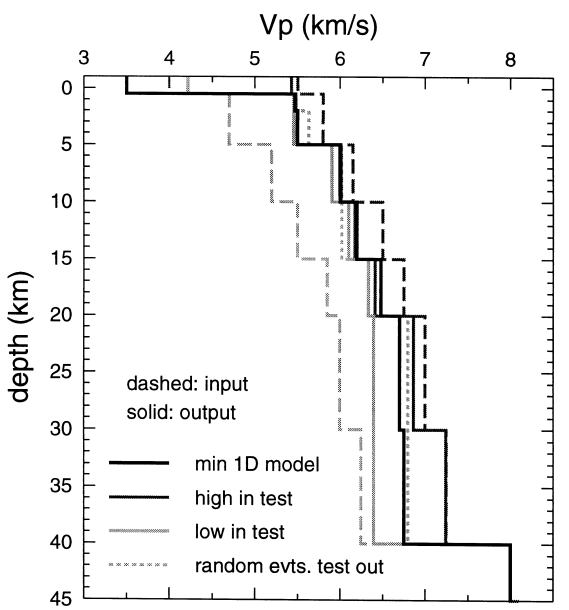

Fig. 4. Tests on the stability of the minimum 1D P-velocity model. The solid black line shows the minimum 1D P-velocity model. The dashed grey lines show the input models for the tests with high and with low initial velocities and the solid grey lines the resulting models after the inversion. Convergence is good between 0.5 and 20 km depth, fair between 20 and 30 km depth, and in the top layer and below 30 km velocities are unconstrained. The dotted grey line shows the resulting velocity model from the inversion with randomly perturbed hypocenters as input.

sparse sampling, as with a few exceptions seismicity terminates at about 25 km. The final minimum 1D P-velocity model (Fig. 3; Table 1) has an average velocity of 6.2 km/s for the upper 30 km of the crust with a fairly constant gradient from 5 to 20 km depth, thus resembling a continental crust with perhaps a little faster-than-average velocity but no unusual features.

Station delays to a minimum 1D model primarily depend on lateral variations in the shallow subsurface although they also map parts of the deeper 3D crustal velocity structure. The resulting station delays (Fig. 3), relative to the reference station in the central part of the area, support the validity of the velocity model by resembling the general near-surface geology. They show the largest positive values (corresponding to true velocities lower than the 1D model velocities) on the thick sediments in the nortwest and large negative values in the east on limestone sequences (Fig. 13). The absolute station delay values tend to be larger at the outside of the network. This is a combination of the effects of local geology and the distribution of azimuths and distances of observations at these stations. Stations in the network center tend to have observations from a wide range of azimuths and distances, which leads to averaging of major 3D effects of the velocity

structure. Stations on the network boundaries have a limited range of observation azimuths and distances; therefore, effects of the three-dimensionality of the velocities will have systematic effects on the station delays.

After inversion for P-velocities, the S-phases were included in the process to jointly invert for a P and S 1D velocity model. Therefore the 441 local earthquakes were relocated with P- and S-data using the minimum 1D P-velocity model and a constant initial V_p/V_s ratio of 1.8. This value was inferred from Wadati diagrams of our data and is in accordance with other studies of the region (e.g. Hatzfeld et al., 1995; Le Meur et al., 1997). The same selection criteria as for the P-data were then applied which yielded 227 events with 2853 P- and 1101 S-observations. During this joint inversion the P-velocities were fixed, but station delays for P- and S-waves, hypocentral parameters, and S-velocities were left floating. The final RMS residual of 0.09 s for P- and S-data is slightly larger than the corresponding value for P-data only (0.08 s); an expected result that correlates with the larger reading errors for S-wave data.

The same tests as for the P-velocity model were performed for the S-model, starting with S-velocities corresponding to $V_p/V_s = 1.7$ and 1.9 and using randomly perturbed hypocenters as input. As for the P-velocity model, velocities are not well constrained in the top layer and below 30 km. The final minimum 1D P- and S-velocity models (Table 1; Fig. 5) show an average V_p/V_s ratio of 1.85 for the top 30 km, with a negative gradient in the top 10 km and slightly increasing values for the depth range of 10 km to 20 km. These apparently well constrained V_p/V_s values are quite high, and at the moment no satisfying interpretation can be given. Maybe the low S-velocities are caused by increased heat-flow in this region of intense crustal deformation, or the presence of fluids at depth.

For seismotectonic interpretations, high-precision hypocentral coordinates and reliable error-estimates are crucial. As we do not have any documented quarry blasts recorded with our network to provide an independent estimate of the location accuracies and uncertainties, we used the output of the tests with randomly perturbed hypocenters and the differences between locations using P only, or P- and S-data and between minimum 1D and 3D model locations to verify the accuracy of our hypocentral coordinates (Fig. 6; Table 2). The average location misfits from the tests with randomized hypocenters and the comparison of hypocentral differences between the locations with and without S-wave data and between the locations from the minimum 1D and the 3D model (discussed below) are consistently small. From these tests we estimate a hypocentral accuracy of about ±500 m in horizontal directions and about ±1000 m in depth for the well locatable events.

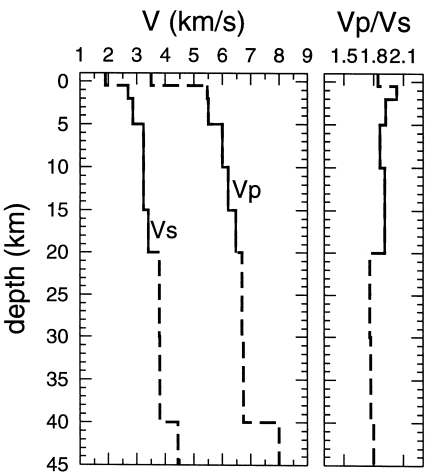

Fig. 5. The minimum 1D P- and S-velocity models and the resulting V_p/V_s ratio. The velocity model is well constrained from 0.5 to 20 km depth (solid line, ±0.2 km/s velocity uncertainty), the surface layer velocity is almost arbitrary and below 30 km, the sparse sampling increases model uncertainty. See Table 1 for tabulated values of V_p and V_s.

5. Seismicity

The general pattern of recorded seismic activity (Fig. 3, all events relocated with the minimum 1D P-velocity model), is similar to the observations of Hatzfeld et al. (1995) during their experiment in 1989. In the southern part of our study area, seismicity appears mostly clustered; north of the south shore of the Gulf of Arta it becomes more evenly distributed, but it is mostly confined to the east of the gulf. The main part of the activity occurs in the region around the KFZ. There it also reaches its

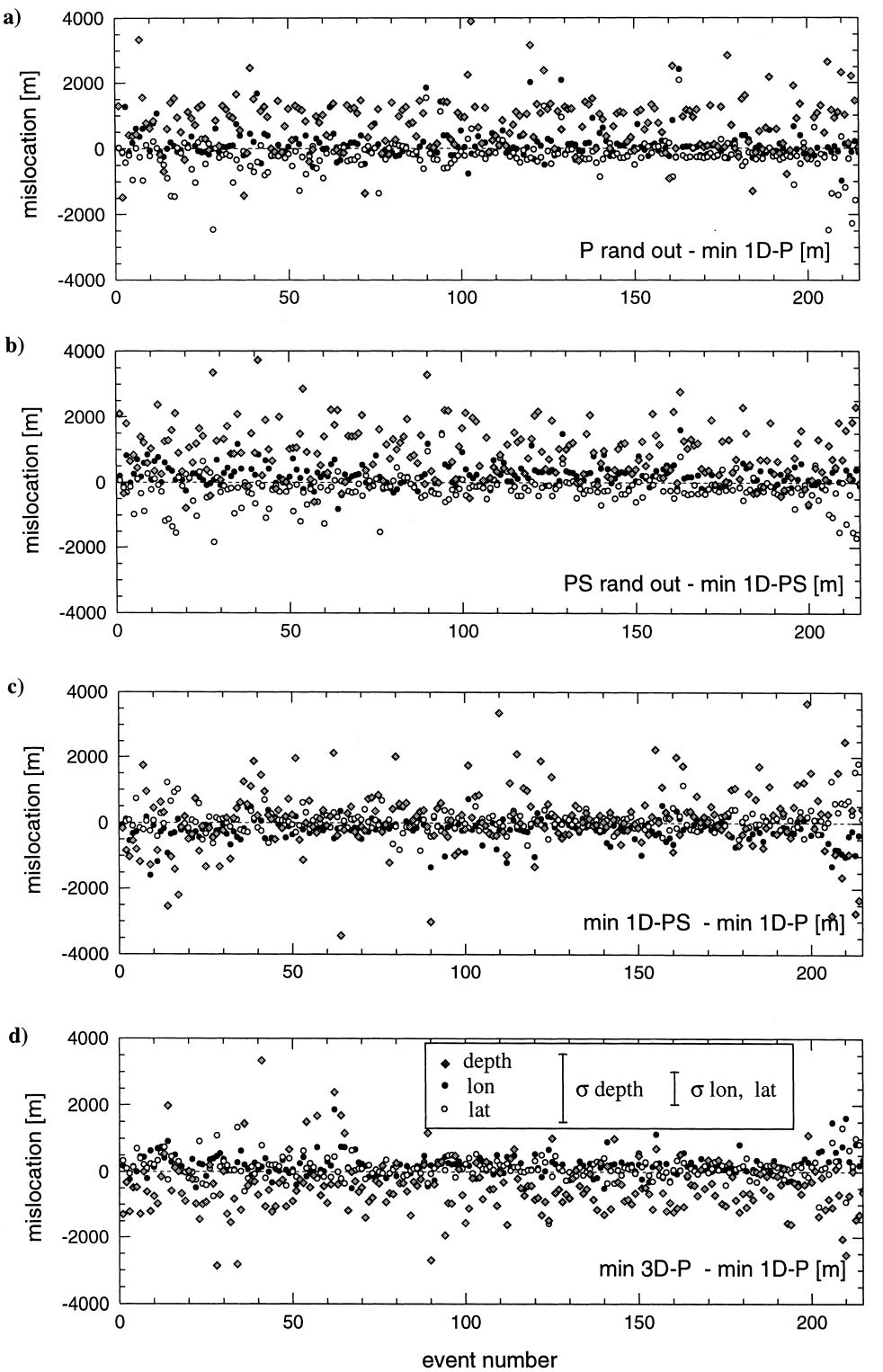
a)
mislocation [m]
4000
2000
0
-2000
-4000
0
50
100
150
200
P rand out - min 1D-P [m]
b)
mislocation [m]
PS rand out - min 1D-PS [m]
c)
mislocation [m]
min 1D-PS - min 1D-P [m]
d)
mislocation [m]
depth
lon
lat
σ depth
σ lon, lat
min 3D-P - min 1D-P [m]
event number

greatest depths, with the exception of one event on the north shore of the Gulf of Arta. This event has 19 P- and 6 S-observations and a depth uncertainty of about ±2 km, inferred from the difference between P- and P- + S-locations. In general, the activity is confined to the top 25 km of the crust. High activity in the top 5 km is observed beneath the Pergandi Mountains (see Fig. 2 for geographic location), with hypocentral depths increasing towards the east in the direction of the KFZ. The events between the Pergandi Mts. and the KFZ appear to deepen towards the southeast. One large cluster of events at intermediate crustal depth lies just outside of our network to the east, south of the Kremaston reservoir (Fig. 2), and the locations are therefore not well constrained. Possibly this activity is induced seismicity linked to the reservoir. Filling of the reservoir is thought to have caused a magnitude 5.6 earthquake in 1966 (Anderson and Jackson, 1987). During the period July to September 1995, the Gulf of Arta and the region north of it remained more or less aseismic, as well as the area southwest of the Pergandi Mountains. No comprehensive magnitude computation has been done so far, but the largest events do not exceed M_L 3.5 and the majority of the recorded events have M_L between 1 and 2.5.

6. 3D tomography

After relocation of all events with the minimum 1D P-model, a selection for a gap $\leq 180^o$ and at least 6 P-readings yielded a data set of 220 events with 2766 P-readings, which were then used in the 3D inversion. No inversion for S-velocities or V_p/V_s is undertaken in this study.

Considering the ray distribution of the selected data, a horizontal grid with 10 × 10 km node spacing covering an area of 100 × 100 km was chosen for this inversion (Fig. 7). Vertical grid spacing is between 5 and 7 km, covering a depth range from the surface to 40 km depth. With this parameterization we can obtain a coarse but reliable image of the 3D crustal structure. The choice of damping values for the 3D inversion was based on a series of tests on the trade-off between model variance (roughness) and data variance (Eberhart-Phillips, 1986). For a large range of damping values, one-iteration inversions were conducted (Fig. 8). A damping value of 50 has been chosen from these tests, as this leads to a significant reduction in the data variance with only a moderate increase in model roughness. Regarding the shape of the curve in Fig. 8, a smaller damping would probably still yield reasonable results. Nevertheless, regarding our grid spacing and ray coverage, we prefer to use a conservative damping. This will lead to a slightly overdamped solution, which has to be kept in mind when interpreting.

A 3D tomographic image is only as good as its resolution estimates, so great care was taken to assess the resolving power of the data set. One very rough estimate of the illumination of the model space is given by the hit count, which sums up the number of rays that contribute to the solution at one node. In SIMULPS the derivative weight sum (DWS) is implemented as a more sensitive measure of the spatial sampling of the model space. The DWS quantifies the relative ray density in the volume of influence of a model node, weighting the importance of each ray segment by its distance to the model node. An even better measure to estimate the quality of the inversion result is the resolution matrix (R). Each row of R describes the dependency of the solution for one model parameter on all the other model parameters. As a first-order diagnostic tool, the diagonal elements of R (RDEs) can be used, as they show the amount of independence in the solution of one model parameter: the larger the RDE for one model parameter, the more independent is the solution for this parameter. For a more detailed discussion on resolution

Fig. 6. Hypocentral uncertainty tests. Open circles: latitude difference, positive means that minimum 1D P-location is to the south; full circles: longitude difference, positive means that minimum 1D P-location is to the west; grey diamonds: depth difference, positive means that minimum 1D P-location is more shallow. The values for σ and average difference are given in Table 2, the approximate size of σ for depth and longitude–latitude is shown with vertical bars. (a) Differences between output of randomized input events test (see text) and minimum 1D model locations for P-phases and model only. (b) Same as (a) for P- + S-phases and model. (c) Differences using only P- and P- + S-phases. (d) Differences between 3D model locations and minimum 1D P-model locations. The outliers (differences >3 km) are mostly events which lie on the border of the network (gap ~180°) or have only 6–8 observations.

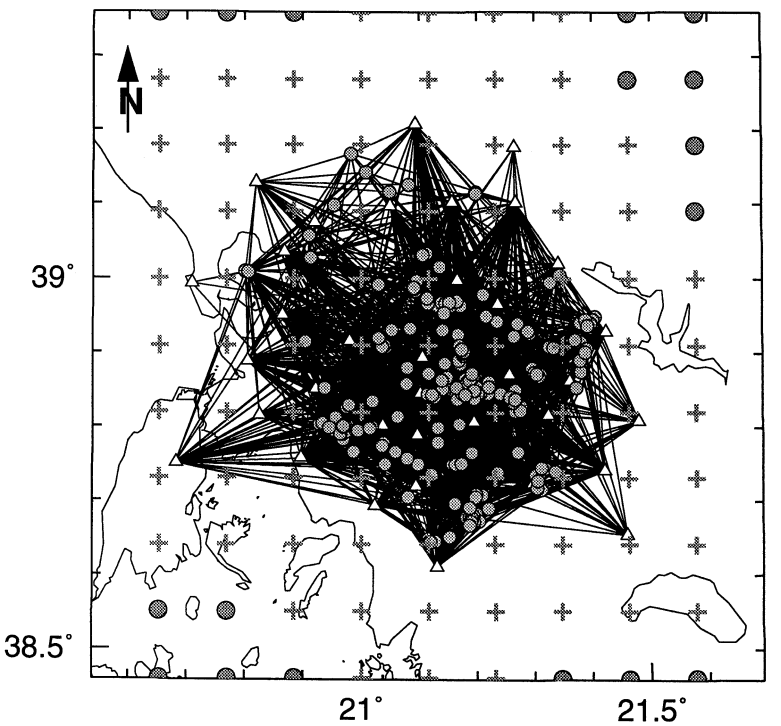

Fig. 7. Horizontal grid design for 3D tomography. Earthquakes used in the inversion are shown as small grey circles, stations as empty triangles and straight rays connecting hypocenters and stations with black lines. The position of the grid nodes for the inversion is shown with grey crosses where the velocities were inverted for, and with large grey circles for nodes where velocities were kept fixed during the inversion. Note that nodes with DWS < 2 were also kept fixed during the inversion. Node spacing is 10 km in either direction. The fixed boundary nodes surrounding this grid are outside the map.

estimates, see e.g. Toomey and Foulger (1989). In this work we choose to define the solution as reliable if the model parameter belongs to an area which is well illuminated, as measured by the DWS (>1000), and shows uniformly high resolution as measured by the RDEs (>0.2). Fig. 9 shows the three above-mentioned quality measures for grid layers 2 and 3, including a white contour which outlines the inferred region of reliable inversion results when the aforementioned criteria are applied. Grid layer 1 encompasses the topography (centered at 2 km above sea level) and is therefore poorly resolved, as only sub-vertical rays sample this layer only below stations.

Another way to estimate the solution quality of a tomographic inversion and at the same time asses the

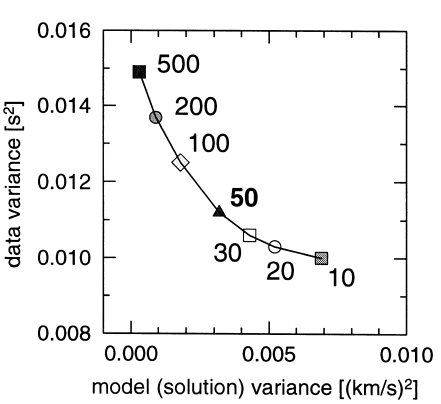

Fig. 8. Model variance plotted versus data variance after one iteration for damping values between 500 and 10. From this trade-off curve a value of 50 is selected as appropriate damping value for the 3D inversion.

Fig. 9. Hit count (top), DWS (middle) and RDE (bottom) for layers 2 and 3. The interpretation of DWS and RDE together is used to derive the area with reliable resolution, surrounded by a white contour. It can be seen that hit count alone gives no information about the reliability of the resolution. See text for further explanations.

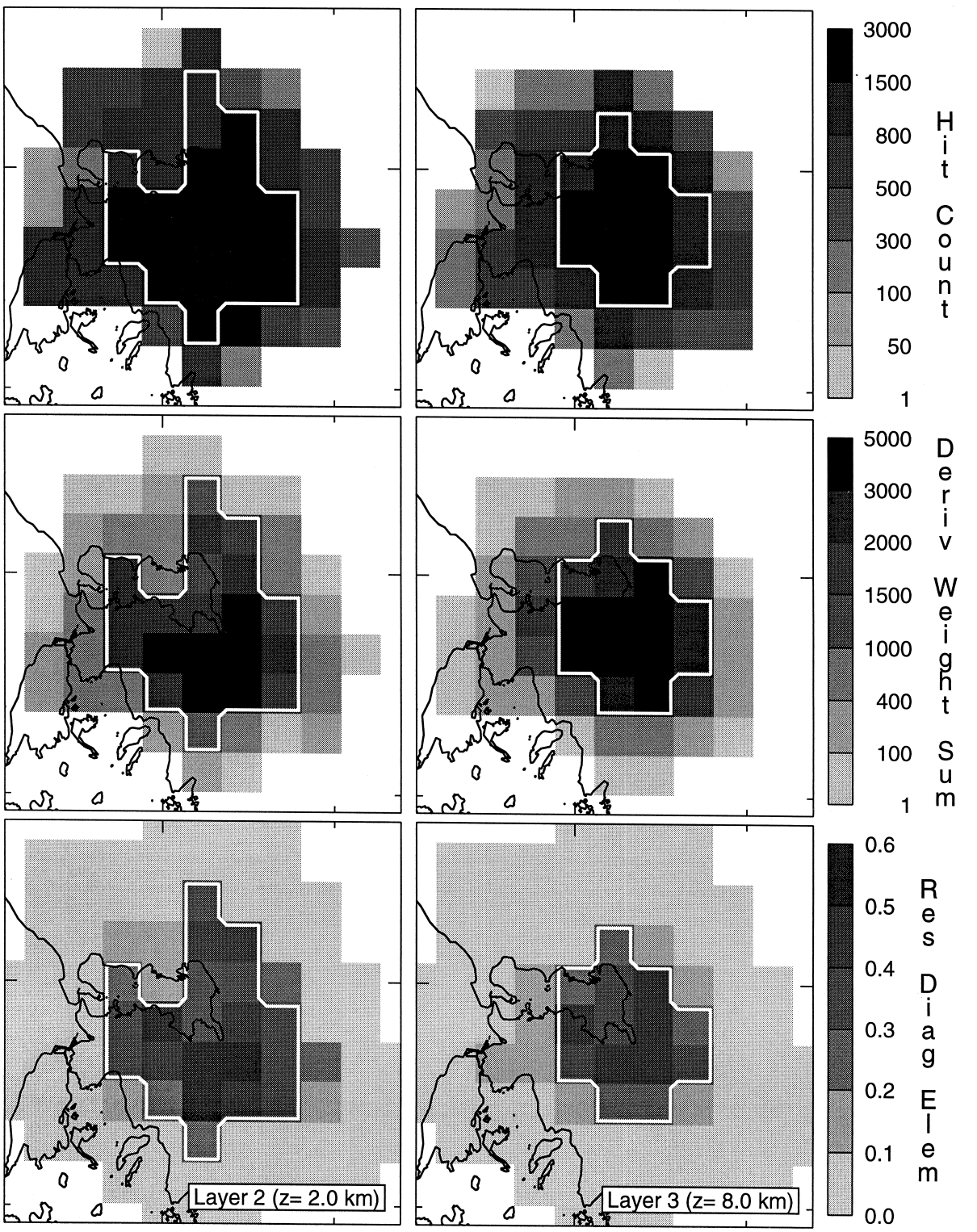
3000
1500
800
500
300
100
50
1
Hit Count
5000
3000
2000
1500
1000
400
100
1
Deriv Weight Sum
0.6
0.5
0.4
0.3
0.2
0.1
0.0
Res Diag Elem
Layer 2 (z= 2.0 km)
Layer 3 (z= 8.0 km)

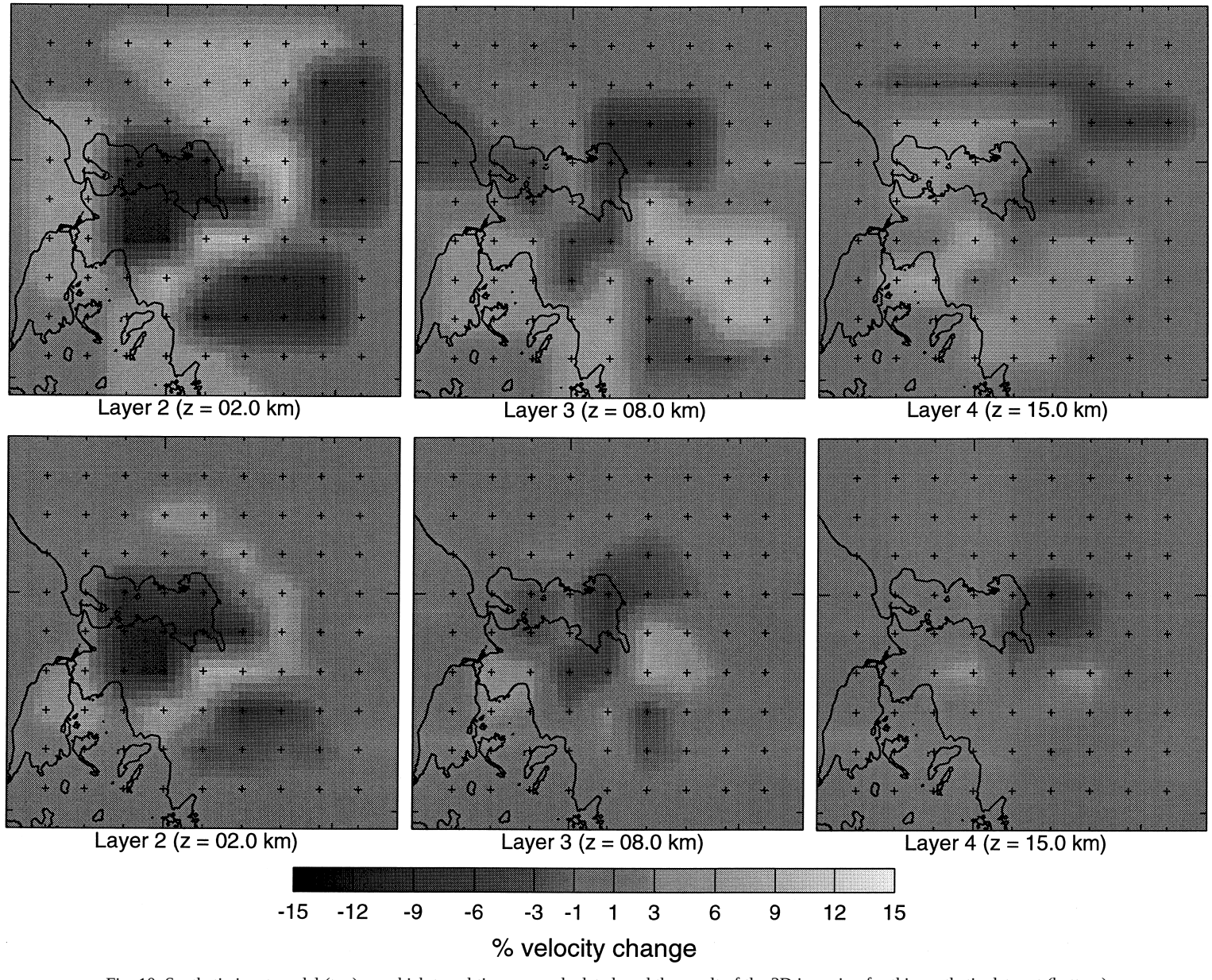

Fig. 10. Synthetic input model (top) on which travel times are calculated, and the result of the 3D inversion for this synthetic data set (bottom).

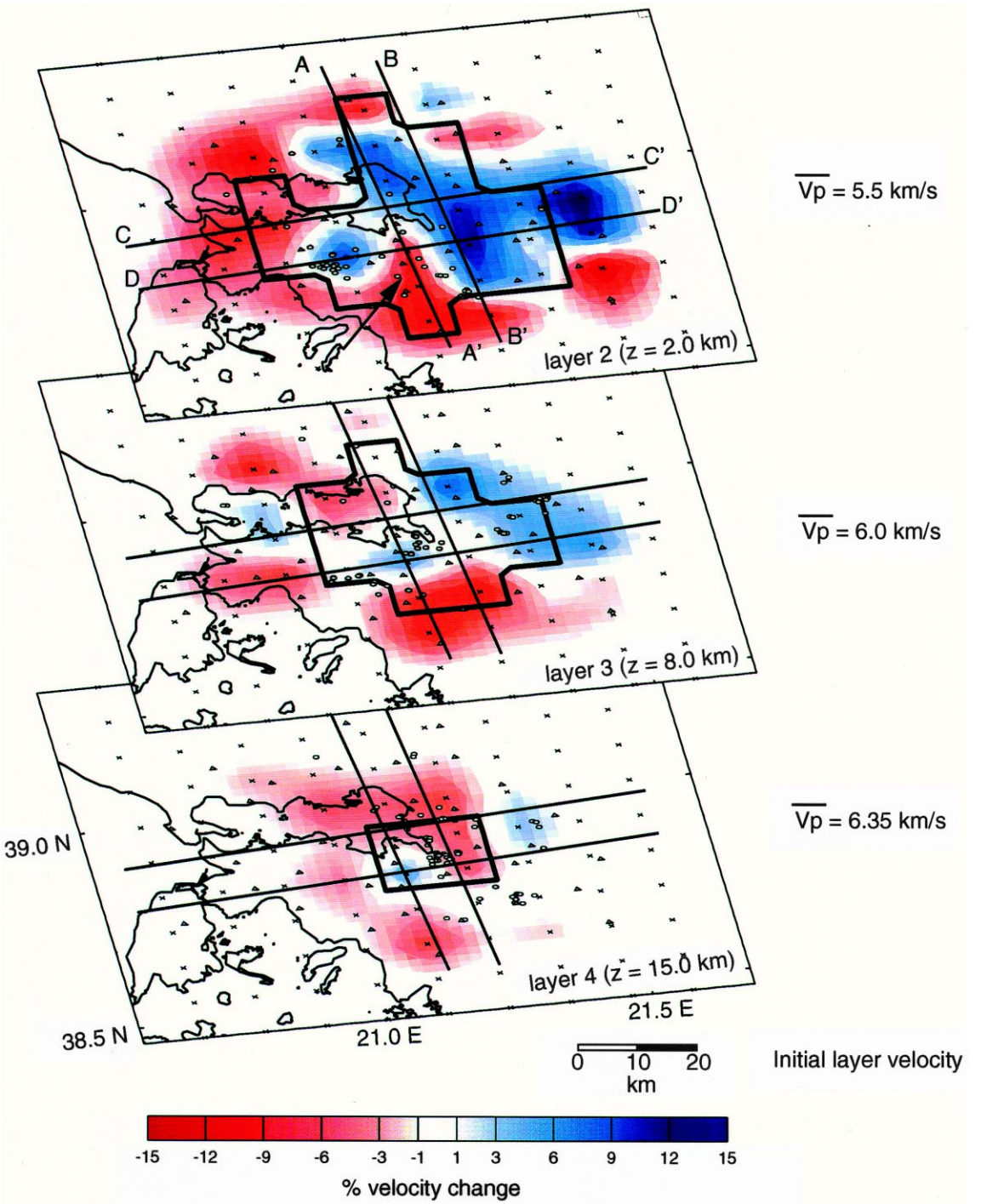

Fig. 11. Velocity perturbations (%) relative to the initial velocity model for the layers centered on 2, 8 and 15 km depth (top to bottom). Red: slower; blue: faster than initial model. The thick black contour denotes the limit of reliable resolution (cells with RDE $\geq$ 0.2 and DWS $\geq$ 1000, see Fig. 9 and text). The inversion grid nodes (10 km spacing) are marked with crosses. Grey triangles: stations; open circles: earthquakes within the layer. The positions of the 4 depth-cross-sections are shown as thin black lines. The arrow on the top plane depicts the location of the low-velocity anomaly mentioned in the text. See text for interpretation.

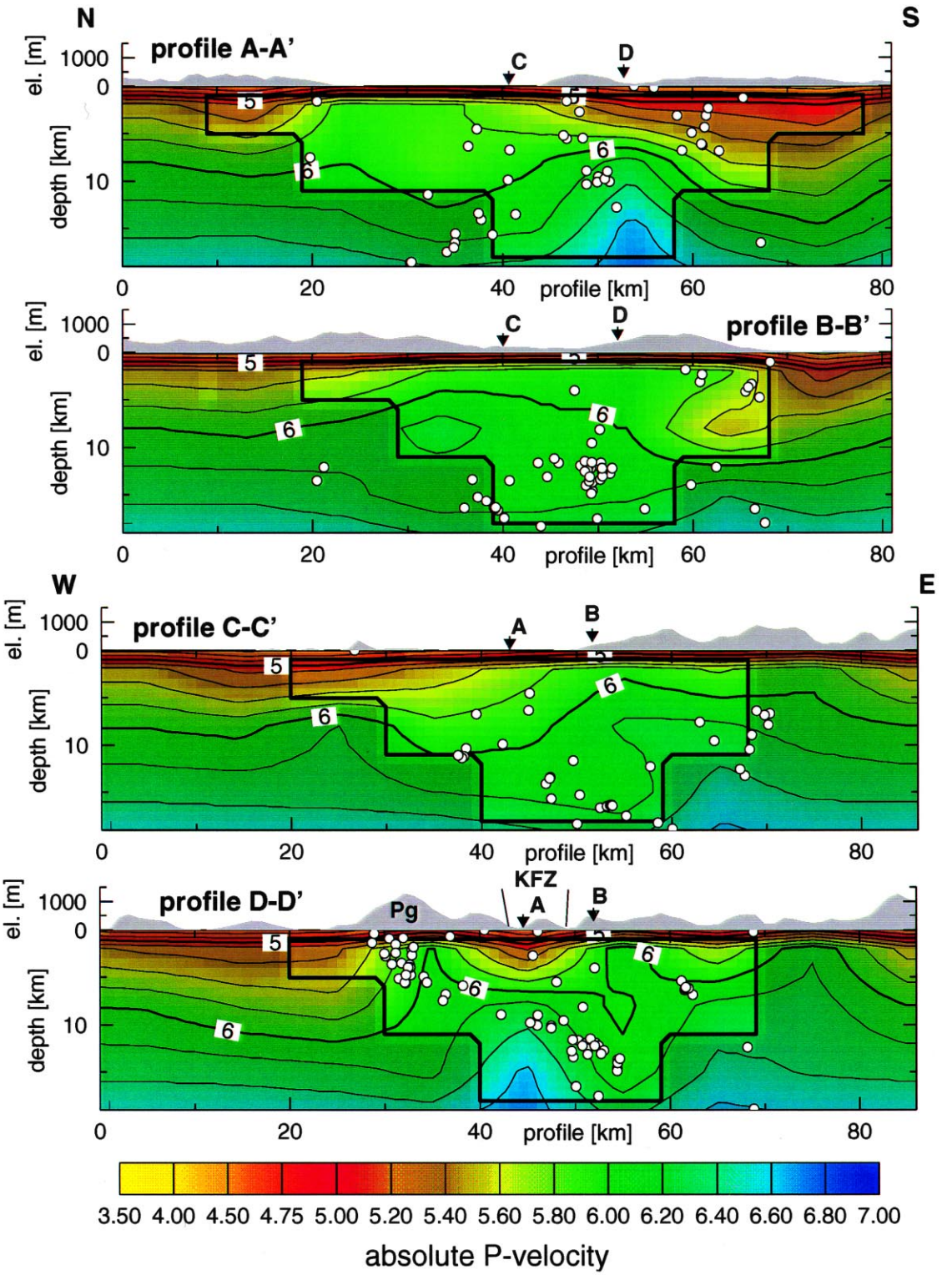
N
S
profile A-A'
C
D
el. [m]
1000
0
depth [km]
10
5
6
0
20
40
profile [km]
60
80
profile B-B'
W
E
profile C-C'
A
B
profile D-D'
KFZ
Pg
3.50 4.00 4.50 4.75 5.00 5.20 5.40 5.60 5.80 6.00 6.20 6.40 6.60 6.80 7.00
absolute P-velocity

effect of the chosen damping parameter on the solution is the inversion of data created by forward ray tracing in a synthetic velocity model. We designed a synthetic model with anomalies similar in size and amplitude to those obtained from the inversion of the real data (Fig. 10), and calculated synthetic travel times with the same source–receiver distribution. These data were then inverted using the same parameterization and control values as for the real data. In the resulting velocity model (Fig. 10) the effect of the damping is apparent in the reduced amplitudes of the recovered anomalies. In grid layers 2 and 3 the structural resolution is good in the areas previously defined to be reliably resolved by evaluating DWS and RDE, in grid layer 4 the resolution in this area is still fair.

According to the synthetic tests and the resolution criteria, the 3D P-velocity structure is well resolved in the central part of the study area to a depth of about 20 km. In Figs. 11 and 12 the outline of the inferred region with reliable results is marked by a thick solid black line. As expected from the chosen gridding and damping, the resolved velocity pattern is relatively smooth and the computed standard errors for well resolved nodes are between 0.02 and 0.04 km/s. It is well known (e.g. Eberhart-Phillips, 1986) that these values tend to underestimate the true velocity error. Regarding the results of the synthetic test it is obvious that we may underestimate the amplitude of anomalies by a few percent. From this we tentatively assume an uncertainty in the final absolute velocity values of $\pm$0.1–0.2 km/s in the well resolved areas.

The scale of the surface geologic structures in the study area (Fig. 13) is on the order of our grid-spacing and smaller. The tomographic results therefore represent a somewhat averaged (or low-pass filtered) image of the crustal velocities. Nevertheless some significant features can be recognized and compared with surface features.

In the upper 10 km we see generally higher P-velocities towards the east, below the foothills of the Pindus Mountains (Fig. 11, layers 2 and 3; Fig. 12, profile C–C′, D–D′), with absolute values between 5.8 and 6.2 km/s. Surface geology of this area is dominated by well exposed flysch (the sedimentary deposits on the flanks of emerging orogens, composed of marls, shales, muds, sandstones, and conglomerates, of variable consolidation) (Fig. 13), which normally exhibit much lower P-velocities (between 3.5 and 4.5 km/s, cf. Gassmann and Weber, 1960). Our results indicate that the flysch cannot be very thick and is underlain by higher-velocity material such as compact limestone, which outcrops to the west of the flysch and east of the Pindus thrust. In profile B–B′ (Fig. 12) the area east of the Gulf of Arta shows very homogeneous velocities of around 6 km/s throughout the well resolved area. The low velocities which penetrate from the south at 5–10 km depth cannot be unambiguously interpreted from these results. They might be the expression of emplaced Triassic evaporites, which are known to exist in this area (e.g. B.P., 1971). The first subsurface layer of the inversion (layer 2) shows a distinct pattern of high- and low-velocity zones. Remarkable are the low velocities in the area of the KFZ south of the Gulf of Arta (depicted by the arrow in Fig. 11), with a sharp boundary to the high velocities in the east. Below the Pergandi Mountains and east of the KFZ high velocities are visible from shallow levels to 5 km depth. On profile D–D′ (Fig. 12) these features can be interpreted as a horst and graben structure in the basement overlain by a thin sedimentary cover on the flanks and a thick sedimentary cover in the graben beneath the area of the KFZ. The low-velocity sediments of this trough overlie a zone of high velocity between 6 km and 18 km depth, also seen on profile A–A′. The general eastward deepening of hypocenters observed in profile D–D′ beneath the Pergandi Mts. and also for the cluster of events east of profile km 60 could be indicating that earthquake activity is occurring on the eastward-dipping listric

Fig. 12. Depth-cross-sections through the 3D P-velocity model. Absolute P-velocities are color-coded and contoured every 0.2 km/s. Hypocenters from $\pm$5 km around the profile are projected onto the profile as open circles. The thick black contour denotes the limit of reliable resolution (see Fig. 8 and text for explanation). Areas with less reliable resolution are shaded. Topography along the profile is plotted on top (scale 3$\times$ exaggerated to depth). The upper two profiles are N–S, the lower two W–E. Crossing points of the profiles are marked with the corresponding letters. *Pg* = Pergandi Mountains; *KFZ* = Katouna fault zone.

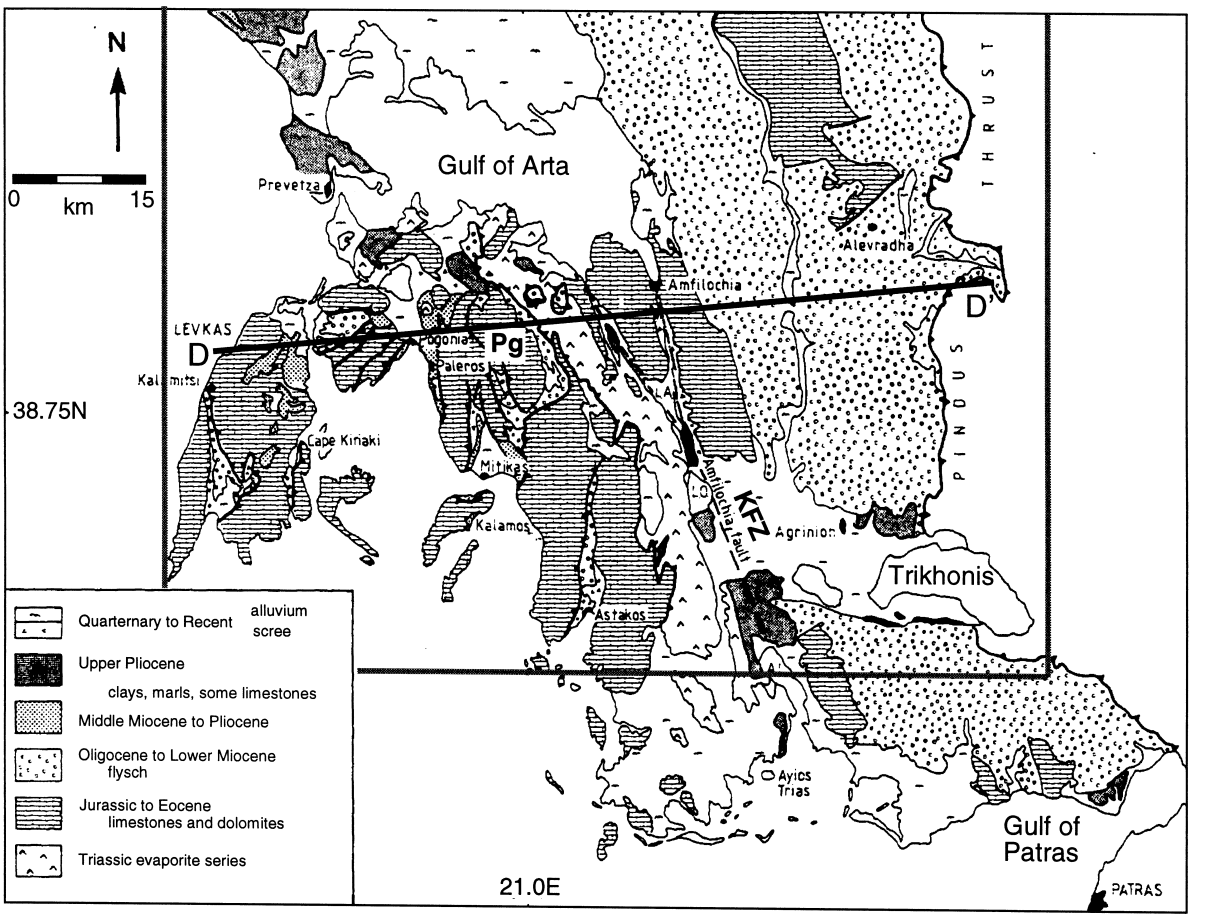

Fig. 13. Simplified geological map of the study area, showing main Neogene units. From Clews (1989). Additionally predominant lithologies are indicated in the legend. The boundary of the tomography planes (grey line) and the location of profile D–D′ (Figs. 9 and 10, black line) are given for reference. The northern boundary of the tomography planes is about 25 km off the top of the map. *Pg* = Pergandi Mountains; *M* = Katouna fault zone (notations of this paper).

thrust faults which formed during the compressional events of the Hellenic orogeny (B.P., 1971; Brooks et al., 1988).

In general, the basement topography in the vicinity of the Pergandi Mts. corresponds with surface topography but shows only little correlation with surface geology. This suggests that the expected sedimentary layers are thin, an interpretation in accordance with geologic models (B.P., 1971). The size (10 km) of our velocity grid, however, does not allow to represent the 3D subsurface structure in sufficient detail to directly correlate and compare it with surface geology. For this purpose, a further tomographic study with a finer velocity grid is planned.

7. Discussion and conclusion

Data from a 3-month field experiment in 1995 were used to compute a minimum 1D P- and S-velocity model and corresponding station delays for the area around the Gulf of Arta in northwestern Greece. This velocity model yields high-quality earthquake locations with average location errors of 500 m horizontally and 1 km vertically. As 1D models are still most commonly used for earthquake location, this model can be used for comparative studies. Due to the improved velocity model and a denser station spacing our location uncertainties are about 5 times smaller than those from Hatzfeld et

al. (1995). Seismic activity in the study area was as high as expected from the observations of Hatzfeld et al. (1995), and the observed microseismicity patterns are similar. The distribution of seismicity appears mostly clustered and apparently is linked to active faults in the region, notably the Katouna fault zone.

With local earthquake delay time tomography we resolve the 3D P-velocity structure of the upper crust. Careful analysis of the resolution capabilities of the data set shows that the velocity structure in the central part of the study area is well resolved on a 10 × 10 km horizontal grid to a depth of about 20 km. E–W-oriented depth-cross-sections image the basement in the area of the KFZ south of the Gulf of Arta as a horst–graben structure, underlain by high-velocity material. The shallow subsurface in the KFZ area consists of relatively low-velocity material, and the eastern part of the Gulf of Arta displays a constant velocity of about 6 km/s extending from the top to 10–15 km depth. Data processing for a dense GPS network operated in 1995 in the study area (Kahle et al., 1997) is under way, and it will be interesting to see whether the basement structures inferred from the 3D velocity image is also visible in the relative motion vectors from GPS observations.

This preliminary study verified the high quality of the local earthquake data set collected during the Akarnania 1995 experiment. Further studies must be undertaken to obtain a more detailed picture of the well resolvable central part of this study area, and to analyze relative locations and focal mechanisms of earthquake clusters to better constrain the position and sense of motion of active faults in this region.

Acknowledgements

We wish to thank all people who helped us maintaining the stations in the field, and whose great efforts were crucial for the success of the Akarnania ’95 experiment: V. Alexandropoulo, Ch. Bärlocher, D. Baumont, A. Blanchard, N. Gourzoulidis, V. Ikonomou, L. Karagianni, N. Karavas, I. Kassaras, G. Kaviris, A. Kepas, J. Könemann, H. Louvari, T. Megel, G. Milonas, J. Riepl, S. Sellami, S. Solarino, E. Terzopoulo, P. Triantafyllidis, B. Urgelli, F. Waldhauser and P. Zweifel. Large parts of the data processing were done with the GIANT software (Rietbrock and Scherbaum, 1998). S. Husen and F. Gräber helped with software and ideas. Most of the figures were done using GMT (Wessel and Smith, 1995). We profited from careful and thorough reviews by C.H. Thurber and W. Spakman. The project was in part founded by ETH project no. 41-2647.5: ‘Present-day crustal dynamics in the Adriatic–Aegean plate boundary zone based on GPS, INSAR and microseismic studies’. Contribution no. 1046, Institute of Geophysics, ETH Zürich.

References

Anderson, H., Jackson, J., 1987. Active tectonics of the Adriatic region. Geophys. J. R. Astron. Soc. 91, 937–983.

Armijo, R., Meyer, B., King, G.C.P., Rigo, A., Papanastassiou, D., 1996. Quaternary evolution of the Corinth rift and its implications for the Late Cenozoic evolution of the Aegean. Geophys. J. Int. 126, 11–53.

B.P. Co Ltd., 1971. The geological results of petroleum exploration in western Greece. Institute for Geology and Subsurface Research 10, 73 pp.

Brooks, M., Clews, J.E., Melis, N.S., Underhill, J.R., 1988. Structural development of Neogene basins in western Greece. Basin Res. 1, 129–138.

Clews, J.E., 1989. Structural controls on basin evolution: Neogene to Quaternary of the Ionian zone, western Greece. J. Geol. Soc. London 146, 447–457.

Eberhart-Phillips, D., 1986. Three-dimensional velocity structure in Northern California Coast Ranges from inversion of local earthquake arrival times. Bull. Seismol. Soc. Am. 76, 1025–1052.

Eberhart-Phillips, D., 1993. Local earthquake tomography: earthquake source regions. In: Iyer, H.M., Hiahara, K. (Eds.), Seismic Tomography: Theory and Practice. Chapman and Hall, London, pp. 613–643.

Evans, J.R., Eberhart-Phillips, D., Thurber, C.H., 1994. User’s manual for SIMULPS12 for imaging V_p and V_p/V_s: a derivative of the ‘Thurber’ tomographic inversion SIMUL3 for local earthquakes and explosions. U.S. Geol. Surv. Open-File Rep. 94-431, 101 pp.

Gassmann, F., Weber, M., 1960. Einführung in die Angewandte Geophysik. Hallwag, Bern, 284 pp.

Hatzfeld, D., Kassaras, I., Panagiotopoulos, D., Amorese, D., Makropoulos, K., Karakaisis, G., Coutant, O., 1995. Microseismicity and strain pattern in northwestern Greece. Tectonics 14, 773–785.

Kahle, H.-G., Muller, M.V., Mueller, St., Veis, G., 1993. The Kephalonia transform fault and the rotation of the Apulian Platform: evidence from satellite geodesy. Geophys. Res. Lett. 20 (8), 651–654.

Kahle, H.-G., Muller, M.V., Geiger, A., Danuser, G., Mueller, St., Veis, G., Billiris, H., Paradissis, G., 1995. The strain field

in NW Greece and the Ionian Islands; results inferred from GPS measurements. Tectonophysics 249, 44–52.

Kahle, H.-G., Peter, Y., Cocard, M., Haslinger, F., Kissling, E., Ansorge, J., Veis, G., Felekis, S., Paradissis, D., Hatzfeld, D., Karakostas, V., 1997. The Adriatic–Aegean plate boundary around the Gulf of Arta, NW Greece: first results from continuous GPS data and a microseismicity survey. EOS 78 (17), Suppl. S321.

King, G., Sturdy, D., Whitney, J., 1993. The landscape geometry and active tectonics of northwest Greece. Geol. Soc. Am. Bull. 105, 137–161.

Kissling, E., 1988. Geotomography with local earthquake data. Rev. Geophys. 26, 659–698.

Kissling, E., 1995. Velest Users Guide. Internal report, Institute of Geophysics, ETH Zurich, 26 pp.

Kissling, E., Ellsworth, W.L., Eberhart-Phillips, D., Kradolfer, U., 1994. Initial reference models in seismic tomography. J. Geophys. Res. 99, 19635–19646.

Kissling, E., Solarino, S., Cattaneo, M., 1995. Improved seismic velocity reference model from local earthquake data in northern Italy. Terra Nova 7, 528–534.

Le Meur, H., Virieux, J., Podvin, P., 1997. Seismic tomography of the Gulf of Corinth: a comparison of methods. Ann. Geofis. 40, 1–24.

Le Pichon, X., Chamot-Rooke, N., Lallemant, S., Noomen, R., Veis, G., 1995. Geodetic determination of the kinematics of central Greece with respect to Europe: implications for eastern Mediterranean tectonics. J. Geophys. Res. 100, 12675–12690.

Mantovani, E., Albarello, D., Tamburelli, C., Babbucci, D., Viti, M., 1997. Plate convergence, crustal delamination, extrusion tectonics and minimization of shortening work as main controlling factors of the recent Mediterranean deformation pattern. Ann. Geofis. 40, 611–643.

Melis, N.S., Burton, P.W., Brooks, M., 1995. Coseismic crustal deformation from microseismicity in the Patras area, western Greece. Geophys. J. Int. 122, 815–836.

Papazachos, C.B., Hatzidimitriou, P.M., Panagiotopoulos, D.G., Tsokas, G.N., 1995. Tomography of the crust and upper mantle in southeast Europe. J. Geophys. Res. 100, 12405–12422.

Reuther, C.D., Ben-Avraham, Z., Grasso, M., 1993. Origin and role of major strike-slip transfers during plate collisions in the central Mediterranean. Terra Nova 5, 249–257.

Rietbrock, A., Scherbaum, F., 1998. The GIANT analysis system. Seis. Res. Lett. 69 (1), 40–45.

Sachpazi, M., Hirn, A., Clement, C., Haslinger, F., Kissling, E., Charvis, P., 1999. Western Hellenic subduction and Cephalonia transform: local earthquakes and plate transport and strain. Phys. Earth Planet. Inter. (submitted).

Thurber, C.H., 1983. Earthquake locations and three dimensional crustal velocity structure in the Coyote lake area, central California. J. Geophys. Res. 88, 8226–8236.

Thurber, C.H., 1993. Local earthquake tomography: velocities and V_p/V_s — theory. In: Iyer, H.M., Hiahara, K. (Eds.), Seismic Tomography: Theory and Practice. Chapman and Hall, London, pp. 563–583.

Toomey, D.R., Foulger, G.R., 1989. Tomographic inversion of local earthquake data from the Hengill–Grensdalur central volcano complex, Iceland. J. Geophys. Res. 94, 17497–17510.

Um, J., Thurber, C.H., 1987. A fast algorithm for two-point seismic ray tracing. Bull. Seismol. Soc. Am. 77, 972–986.

Wessel, P., Smith, W.H.F., 1995. New version of the Generic Mapping Tools released. EOS 76, 329.